

MODEL REFERENCE ADAPTIVE CONTROL FOR MAXIMUM POWER POINT TRACKING IN PV SYSTEMS

N. Vyshnavi¹, KBVSR. Subramanyam²

¹PG student [PE&ES], Department of EEE, SR Engineering College, Telangana State, India

²Associate Professor, Department of EEE, SR Engineering College, Telangana State, India

ABSTRACT

This paper proposes adaptive control architecture for maximum power point tracking (MPPT) in photovoltaic systems. Photovoltaic systems provide promising ways to generate clean electric power. MPPT technologies have been used in photovoltaic systems to deliver the maximum power output to the load under changes of solar insolation and solar panel's temperature. To improve the performance of MPPT, this thesis proposes a two-layer adaptive control architecture that can effectively handle the uncertainties and perturbations in the photovoltaic systems and the environment. The first layer of control is ripple correlation control (RCC), and the second layer is model reference adaptive control (MRAC). By decoupling these two control algorithms, the control system achieves the maximum power point tracking with shorter time constants and overall system stability. To track the maximum power point as the solar insolation changes, the RCC algorithm computes the corresponding duty cycle, which serves as the input to the MRAC layer. Then the MRAC algorithm compensates the under-damped characteristics of the power conversion system: the original transfer function of the power conversion system has time-varying parameters, and its step response contains oscillatory transients that vanish slowly. Using the Lyapunov approach, an adaption law of the controller is derived for the MRAC system to eliminate the under-damped modes in power conversion.

Keywords: Photovoltaic system, maximum power point tracking, model reference adaptive control and ripple correlation control.

1. INTRODUCTION

Photovoltaic systems are a critical component in addressing the national mandates of achieving energy independence and reducing the potentially harmful environmental effects caused by increased carbon emissions. Due to variations in solar insolation and environmental temperature, photovoltaic systems do not continually deliver their theoretical optimal power unless a maximum power point tracking (MPPT) algorithm is used. MPPT algorithms are designed in order for the photovoltaic system to adapt to environmental changes so that optimal power is delivered. Typically, MPPT algorithms are integrated into power electronic converter systems, where the duty cycle of the converter is controlled to deliver maximum available power to the load [1], [2].

Several MPPT algorithms have been reported in the literature. The most common of these algorithms is the perturb and observe (P&O) method [3]–[5]. This control strategy requires external circuitry to repeatedly perturb the array voltage and subsequently measure the resulting change in the output power. While P&O is inexpensive and relatively simple, the algorithm is inefficient in the steady state because it forces the system to oscillate around the maximum power point (MPP) instead of continually tracking it. Furthermore, the P&O algorithm fails under rapidly changing environmental conditions, because it cannot discern the difference between changes in power due to environmental effects versus changes in power due to the inherent perturbation of the algorithm [6]. The incremental conductance (INC) method uses the fact that the derivative of the array power with respect to the array voltage is ideally zero at the MPP (see Fig. 1), positive to the left of the MPP, and negative to the right of the MPP. The INC method has been shown to perform well under rapidly changing environmental conditions, but at the expense of increased response times due to complex hardware and software requirements [7].

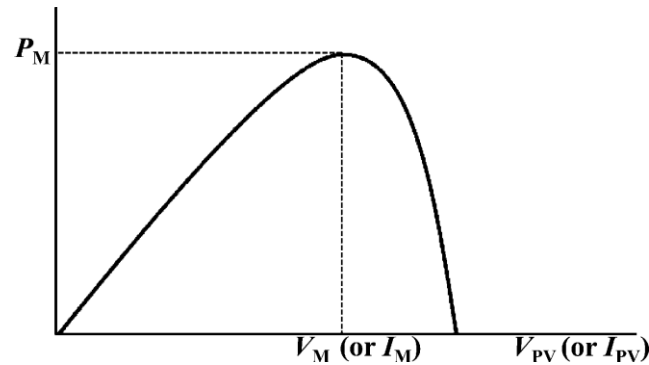


Fig- 1: Power–voltage characteristics of photovoltaic systems.

The fractional open-circuit voltage (FOCV) method uses an approximate relationship between V_{OC} , the open-circuit voltage of the array, and V_M , the array voltage at which maximum power is obtained, to track the MPP [8]. Like P&O, the FOCV algorithm is inexpensive and can be implemented in a fairly straight-forward manner. However, the FOCV method is not a true MPP tracker since the assumed relationship between V_{OC} and V_M is only an approximation. Fuzzy logic and neural network-based algorithms have demonstrated fast convergence and high performance under varying environmental conditions, but the implementation of these algorithms can be undesirably complex [9], [10]. To this end, a general problem associated with MPPT algorithms is the transient oscillations in the system's output voltage after the duty cycle is rapidly changed in order to track the MPP [7]. Thus, the ideal MPPT control algorithm would be simple and inexpensive, and would demonstrate rapid convergence to the MPP with minimal oscillation in the output voltage.

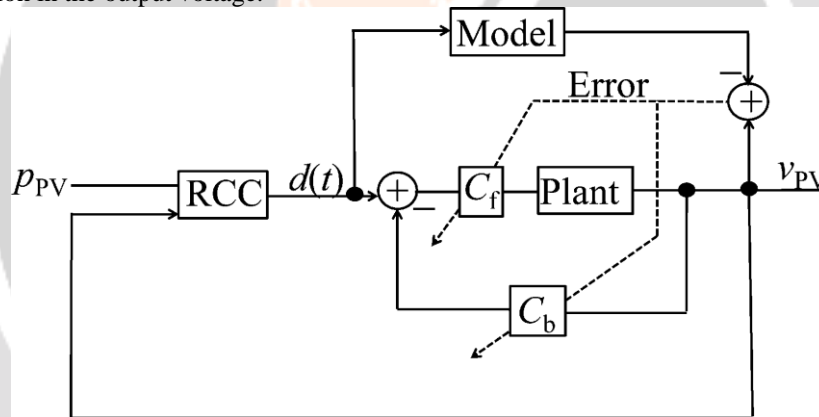


Fig- 2: Proposed MPPT control architecture.

This paper develops a two-level MPPT control algorithm that consists of ripple correlation control (RCC) [11]–[14] in the first level and model reference adaptive control (MRAC) [15], [16] in the second level. As seen in Fig. 2, in the first control level the array voltage v_{PV} and power p_{PV} serve as the inputs to the RCC unit. The RCC unit then calculates the duty cycle of the system, $d(t)$, to deliver the maximum available power to the load in the steady state. In the second control level, the new duty cycle calculated from the RCC unit is routed into an MRAC architecture, where the dynamics of the entire photovoltaic power conversion system, or the plant, are improved to eliminate any potential transient oscillations in the system's output voltage. Transient oscillations in the system's output voltage can result after the duty cycle has been updated to account for rapidly changing environmental conditions. To prevent the plant from displaying such oscillations, a critically damped system is implemented as the reference model in Fig. 2. During adaptation, the error between the plant and reference model is utilized to tune the parameters in the feed forward and feedback controllers, C_f and C_b , respectively. Properly tuning the controller parameters enables the output of the plant to match the output of the reference model, at which point the error converges to zero and the maximum power is obtained. Both the theoretical and simulation results demonstrate convergence to the optimal power point with elimination of underdamped responses that are often observed in photovoltaic power converter systems.

The proposed two-level controller structure can reduce the complexity in system control, with RCC mainly handling the “slow” dynamics and MRAC handling the “fast” dynamics. The previous literature has proven the stability of RCC and MRAC, respectively. Although coupling two stable subsystems will not necessarily lead to the

stability of the overall system, our proposed two-level structure can effectively decouple the RCC and MRAC levels in stability analysis, because the time constants of the two control algorithms used here are significantly disparate.

This paper focuses mostly on the MRAC level of the proposed control architecture. In a sequel paper (in preparation), we will provide a comprehensive analysis validating the coupling of MRAC with RCC. The rest of this paper is organized as follows: Section II provides the problem context for MPPT of photovoltaic systems as well as the background for the dynamics of the converter system. Section III describes the proposed two-level control architecture for MPPT. Results and discussion are given in Section IV followed by concluding remarks in Section.

2. SYSTEM DESCRIPTION

2.1. PV Characteristics

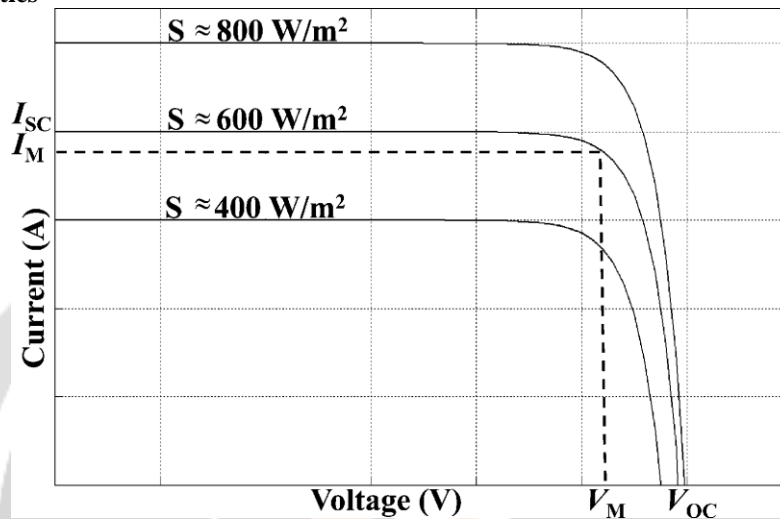


Fig- 3: Current–voltage characteristics of photovoltaic systems under various levels of solar insolation.

Fig. 3 presents the current–voltage ($I-V$) characteristics of photovoltaic systems under various levels of solar insolation. The MPP occurs at the so-called “knee” of the $I-V$ curve, (V_M, I_M) : when either V_M or I_M is achieved, the maximum available power P_M is obtained. A photovoltaic system can regulate the voltage or current of the solar panel using a dc–dc converter interfaced with an MPPT controller to deliver the maximum allowable power [17], [18].

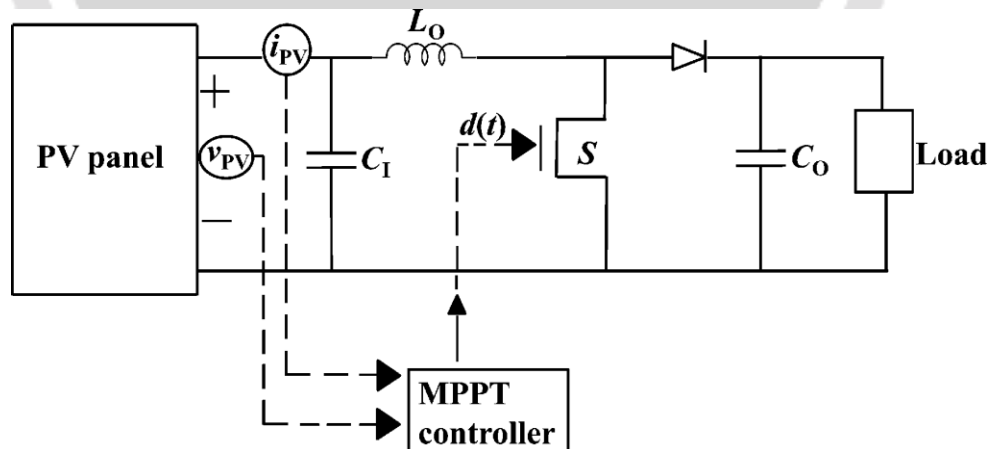


Fig- 4: MPPT controller of a photovoltaic boost converter system.

Fig. 4 shows the integration of such a system where a boost converter is utilized to deliver optimal power to the load. Depending on the application, other power converter topologies may be used in place of the boost converter. In the boost converter system shown in Fig. 4, the MPPT controller senses the voltage and current of the solar panel and yields the duty cycle d to the switching transistor S . The duty cycle of the transistor is related to the array voltage through

$$v_{PV} = i_{PV} R_O (1 - d)^2 \tag{1}$$

where v_{PV} and i_{PV} are the array voltage and current, respectively, and R_O is the load resistance. Both the array voltage and current consist of dc (average) terms, V_{PV} and I_{PV} , as well as ripple terms, \hat{v}_{PV} and \hat{i}_{PV} . The goal then is to design a controller that continually calculates the optimal value of the duty cycle so that V_{PV} tracks V_M (or I_{PV} tracks I_M) and thus delivers the maximum available power.

2.2. Converter Dynamics

The relationship (1) provides the foundation for conventional MPPT algorithms to compute the converter’s duty cycle in steady states. However, to optimize transient responses, the MPPT control must consider the dynamics between the duty cycle and array voltage. Since transient oscillations are undesired and can lead to inefficient operation of the system, the MPPT control needs to eliminate transient oscillations in the array voltage after the duty cycle has been updated to account for changing environmental conditions. A detailed dynamic model of the boost converter can be found in [19]. To simplify the analysis of the system’s transient response, we consider a small signal equivalent circuit (see Fig. 5) as suggested in [7].

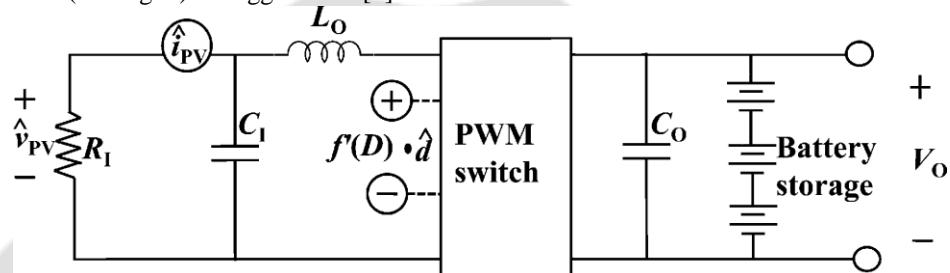


Fig- 5: Small signal equivalent circuit of photovoltaic power conversion system.

A resistor R_1 is used to model the solar array with a small signal array voltage \hat{v}_{PV} and small signal array current \hat{i}_{PV} across its terminals. We now derive the transfer function from the control signal (duty cycle) to the array voltage in small signal operation around an operating point. This transfer function characterizes the dynamics of the system. It should be noted that the dynamic model in Fig. 5 shows in the load of the boost converter a storage battery, which is practical for photovoltaic systems. While this representation will change the value of v_{PV} given $i(1)$ and move the operating point in the steady-state response, it will have little effect on the system’s frequency response for the range of frequencies near the natural frequency, where we see resonances or under damped oscillations. Therefore, we ignore the dynamics of the battery in the derivation of the transfer function from the duty cycle to the array voltage in small signal operation. In analyzing Fig. 5, we have the following relationship in the frequency domain or s -domain:

$$\frac{\hat{v}_{PV}(s)}{R_1} + s\hat{v}_{PV}(s)C_1 = \frac{f'(D)\hat{d}(s) - \hat{v}_{PV}(s)}{sL_0} \tag{2}$$

where s is the Laplace variable, \hat{d} represents the small signal variation around the converter’s duty cycle D at the operating point, $\hat{d}(s)$ and $\hat{v}_{PV}(s)$ are the Laplace transforms of $\hat{d}(t)$ and $\hat{v}_{PV}(t)$, respectively, $f(D)$ is the relationship between the operating duty cycle, D , and the steady-state dc input voltage of the boost converter V_{PV} , $f'(D)$ is the derivative of $f(D)$ with respect to the duty cycle at the operating point D . From (2), we can obtain

$$\frac{\hat{v}_{PV}(s)}{\hat{d}(s)} = \frac{f'(D)}{L_0 C_1 s^2 + \frac{L_0}{R_1} s + 1} \tag{3}$$

It is known that

$$f(D) = V_{PV} = (1 - D)V_O \tag{4}$$

where V_O is the steady-state dc output voltage of the boost converter. The relationship (4) assumes that the dc steady-state relation between $f(D)$ and V_O is unaffected by the transient switching action. From (4), we have $f'(D) = -V_O$ and thus (3) turns to

$$\frac{\hat{v}_{PV}(s)}{\hat{d}(s)} = \frac{-V_O}{s^2 + \frac{1}{R_1 C_1} s + \frac{1}{L_0 C_1}} \tag{5}$$

The minus sign in (5) indicates that decreasing the duty ratio will increase the panel voltage. The parasitic components of the power stage are not considered in this analysis, which is consistent with previous work on modeling the dynamics of photovoltaic integrations with dc–dc converters [20].

The aforementioned transfer function is derived from a linearized version (see Fig. 5) of the nonlinear system in Fig. 4, around a single operating point. As solar insolation varies, the operating point of the system will vary thereby changing the effective values of the parameters in (5), specifically the R_l . To illustrate the effect of R_l on the system, we can analyze the denominator of (5) in the canonical form

$$s^2 + 2\zeta\omega_n s + \omega_n^2 \tag{6}$$

where ω_n is the natural frequency and ζ the damp ratio. Comparing (6) with the denominator of (5), we have $\zeta = 1/2R_l\sqrt{L0/C1}$ When the damping ratio ζ is less than 1, the system is underdamped and presents oscillations in its step responses. To prevent the underdamped oscillations, an adaptive controller is proposed to regulate the dynamics of the closed-loop system or controlled plant. The goal is to tune the damping ratio of the controlled plant to approach 1 so that the system is critically damped. While it is possible to adjust the value of R_l to yield a critically damped system for a single operating point, a fixed R_l cannot keep the system critically damped for varying operating conditions.

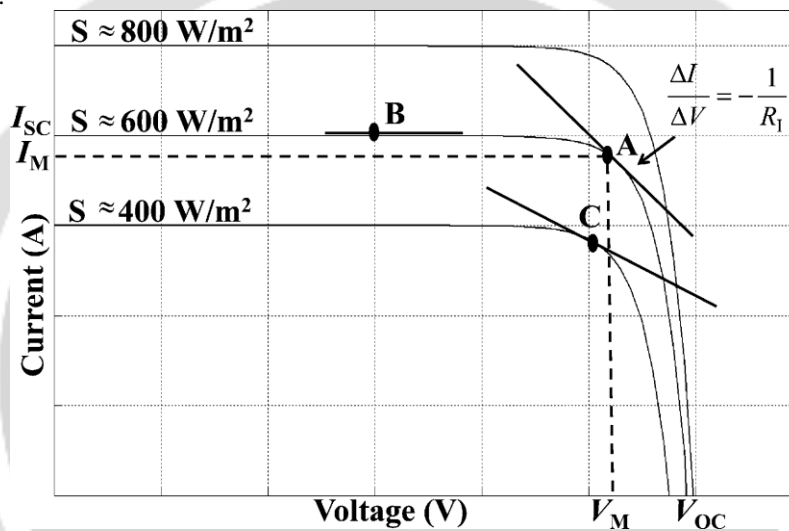


Fig- 6: Current–voltage characteristics of a solar panel with varying R_l superimposed over the graph.

Fig. 6 illustrates current–voltage characteristics for a photovoltaic array at three different levels of solar insolation: 400, 600, and 800 W/m^2 . As described in [20], the value of R_l for the photovoltaic array can be determined by the slope tangential to the operating point of the system.

$$\frac{1}{R_l} \approx -\frac{\Delta I}{\Delta V} \tag{7}$$

The MPP for the curve related to 600 W/m^2 is denoted by point A, i.e., point (V_M, I_M) in Fig. 6. The value of R_l at point A can be inferred as the magnitude of the inverse slope of the line tangential to point A, as suggested by (7). If the operating point moves from point A to point B, under constant solar insolation, it is clear that the value of R_l will change. Furthermore, if the operating point moves from point A to point C, which is the MPP for a solar insolation of 400 W/m^2 , again a different value for R_l is obtained. Thus, even at a new MPP, there is no guarantee that the operating R_l will be equal to the previous optimal R_l . Moreover, there is no guarantee that the operating optimal R_l will deliver a critically damped system. We therefore propose a two-level controller to track the MPP. In the first control level, RCC will be used to force the operating point to the optimal R_l . In the second level, MRAC will be used to optimize the dynamics of the converter so that optimal R_l also delivers a critically damped system (with $\zeta = 1$), in spite of any changes in solar insolation.

3. PROPOSED MPPT ALGORITHM

We propose a two-level adaptive control algorithm for MPPT (see Fig. 2). In the first control level, RCC is utilized to calculate the duty cycle of the converter, which is expected to deliver maximum available power to the load in the steady state. In the second control level, anMRAC structure regulates the dynamics of the converter in

response to the duty cycle calculated from RCC, preventing the array voltage from transient oscillations after changes in solar insolation. The RCC level is responsible to handle changes in solar insolation, and the tuning process of RCC should be fast enough to catch up to the changes in solar insolation. Therefore, the time constant of RCC is required to be smaller than that of the dynamics of insolation changes. In comparison, MRAC is responsible to maintain optimal damping characteristics of the converter whose time constant is much smaller than that of environmental changes. The tuning process of MRAC must be fast enough to catch up to the changes in the operating point of the converter and the responses of RCC. Therefore, the time constant of MRAC is required to be much smaller than that of the RCC. The significant difference between these two time constants allows us to decouple the analyses for RCC and MRAC, and thus greatly simplifies the overall control design. Since RCC is well studied in the literature, this section focuses mostly on the MRAC level of the two-level adaptive control (see Section III-B). We provide only a brief introduction of RCC in Section III-A, but in a sequel paper we will give a more comprehensive analysis on validating the coupling of RCC and MRAC.

3.1. Ripple Correlation Control

The RCC calculates the duty cycle that delivers the maximum power to the load in the steady state. The main innovation of RCC is to use the switching ripple inherent to the converter to perturb the system and thus track the MPP [14]. The RCC is essentially an improved version of the P&O method [3]–[5] except that the perturbation is inherent to the converter. Such a methodology is advantageous because it negates the necessity for external circuitry to inject the perturbation. In addition, RCC has been proven to converge asymptotically to the MPP with minimal controller complexity and straight-forward circuit implementation [14]. The RCC is based on the observation that the product of the time-based derivatives of the array voltage (v_{PV}) and power (p_{PV}) will be greater than zero to the left of the MPP, less than zero to the right of the MPP, and exactly zero at the MPP (see Fig. 1)

$$\frac{dp_{PV}}{dt} \frac{dv_{PV}}{dt} > 0 \quad \text{when } V_{PV} < V_M \quad (8)$$

$$\frac{dp_{PV}}{dt} \frac{dv_{PV}}{dt} < 0 \quad \text{when } V_{PV} > V_M \quad (9)$$

$$\frac{dp_{PV}}{dt} \frac{dv_{PV}}{dt} = 0 \quad \text{when } V_{PV} = V_M \quad (10)$$

These observations lead to the control law derived in [11]

$$\frac{dd(t)}{dt} = k \frac{dp_{PV}}{dt} \frac{dv_{PV}}{dt} \quad (11)$$

where k is a constant of negative gain. The control law (11) can be qualitatively described as follows: if v_{PV} increases and there is a resulting increase in p_{PV} , the system's operating point is to the left of the MPP (see Fig. 1) and therefore d should decrease—causing an increase of v_{PV} according to (1); if p_{PV} decreases after an increase in v_{PV} , then the system's operating point is to the right of the MPP (see Fig. 1) and thus d should increase in order to reduce v_{PV} . From inspection of (10) and (11), the goal then is to drive the time-based derivative of d to zero so that maximum power is obtained. As established in [11]–[14], RCC has a well-developed theoretical basis and has been mathematically proven to yield the optimal value of the duty cycle in order to deliver maximum power in the steady state. The advantage of RCC over conventional algorithms such as P&O, is that in the steady-state RCC converges to the MPP while P&O oscillates around the MPP. Relative to fuzzy logic and neural networks, RCC is advantageous due to its simple implementation as well as its low cost.

In addition to steady-state analysis, one must also consider the transient response of the boost converter system shown in Fig. 4 so that the controller can rapidly converge to the theoretical MPP with minimal oscillation. In the next section, an MRAC algorithm is proposed to prevent the array voltage from exhibiting an under damped response.

3.2. Proposed MRAC Method

In the previous section, RCC is used to calculate the duty cycle aimed at delivering the maximum available power in the steady state. It is also desired that the system converges to the MPP swiftly during changes in solar insolation. As shown in (5), the relationship between the array voltage and the converter duty cycle is a highly dynamic process. Since the operating point will vary as solar insolation varies, it is not guaranteed that the array

voltage exhibits critically damped behavior without adaptive control. The MRAC architecture proposed here is to maintain a critically damped behavior of the array voltage.

The basic idea of MRAC is to design an adaptive controller so that the response of the controlled plant remains close to the response of a reference model with desired dynamics, despite uncertainties or variations in the plant parameters. The proposed architecture of MRAC is shown in Fig. 7.

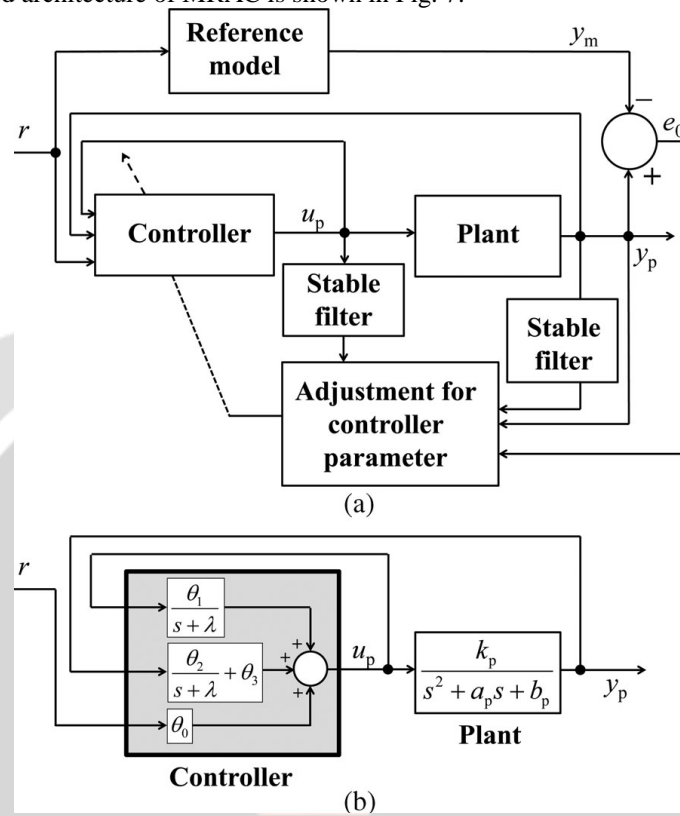


Fig- 7: (a) Proposed MRAC strucutre. (b) Controller structure in the proposed MRAC.

The input to the overall system, $r(t)$, is the change in duty cycle calculated in Section III-A using RCC. The plant model in Fig. 7 corresponds to the transfer function in (5). However, for convenience, we change its sign (by multiplying -1 to it) so that the plant model has only positive coefficients. We use $u_p(t)$ and $y_p(t)$ to represent the input and output of the plant, respectively, and reexpress the plant model as

$$G_p(s) = \frac{y_p(s)}{u_p(s)} = \frac{k_p}{s^2 + a_p s + b_p} \tag{12}$$

where the values and meanings of k_p , a_p , and b_p can be implied from (5). The reference model is chosen to exhibit desired output $y_m(t)$ for input $r(t)$

$$G_m(s) = \frac{y_m(s)}{r(s)} = \frac{k_m}{s^2 + a_m s + b_m} \tag{13}$$

where k_m is a positive gain, and a_m and b_m are determined so that the reference model delivers a critically damped step response. The control objective is to design $u_p(t)$ so that $y_p(t)$ asymptotically tracks $y_m(t)$.

In the following, we take four steps to derive the adaptation law for controller parameters in MRAC: 1) choosing the controller structure; 2) finding state-space expressions for the controlled plant and the reference model; 3) constructing error equations; and 4) deriving an adaptation law for MRAC using the Lyapunov method.

1) **Controller Structure:** To achieve the control objective, we use the controller structure shown in Fig. 7(b). The expression for the controller is

$$\begin{aligned}
 u_p &= \theta_0 r + \theta_1 \frac{1}{s + \lambda} u_p + \theta_2 \frac{1}{s + \lambda} y_p + \theta_3 y_p \\
 &= \theta_0 r + \theta_1 w_1 + \theta_2 w_2 + \theta_3 y_p = \theta^T w
 \end{aligned}
 \tag{14}$$

where $\theta = [\theta_0, \theta_1, \theta_2, \theta_3]^T$ is the parameter vector of the controller, w is defined as $[r, w_1, w_2, y_p]^T$ with $w_1 \equiv 1/(s+\lambda u_p)$ and $w_2 \equiv 1/(s+\lambda y_p)$, and $1/(s+\lambda)$ is a stable filter with an arbitrarily chosen $\lambda > 0$. Equivalently, w_1 and w_2 are determined by

$$\begin{aligned}
 \dot{w}_1 &= -\lambda w_1 + u_p \\
 \dot{w}_2 &= -\lambda w_2 + y_p
 \end{aligned}
 \tag{15}$$

It is shown in [16] that the controller structure (14) is adequate to achieve the control objective: it is possible to make the transfer function from r to y_p equal to G_m . Specifically, $y_p(s)/r(s)$ equals $y_m(s)/r(s)$ when θ equals $\theta^* = [\theta_0^*, \theta_1^*, \theta_2^*, \theta_3^*]^T$ with

$$\begin{aligned}
 \theta_0^* &= \frac{k_m}{k_p} \\
 \theta_1^* &= a_p - a_m \\
 \theta_2^* &= \frac{(a_p - a_m)(-\lambda^2 + \lambda a_p - b_p)}{k_p} \\
 \theta_3^* &= \frac{b_p - b_m + (a_p - a_m)(\lambda - a_p)}{k_p}
 \end{aligned}
 \tag{16}$$

2) **State-Space Expressions of the Controlled Plant and the Reference Model:** Let $\{A_p, B_p, C_p\}$ be a minimal realization of the plant $G_p(s)$

$$\begin{aligned}
 \dot{x}_p &= A_p x_p + B_p u_p \\
 y_p &= C_p x_p
 \end{aligned}
 \tag{17}$$

where x_p is a 2-D state vector. Considering the dynamics of the controller, i.e., (14) and (15), the closed-loop system with the plant and controller in the loop can be described by the following state-space expression:

$$\begin{aligned}
 \dot{x}_{pe} &= A_{pe} x_{pe} + B_{pe} \theta_0^* r + B_{pe} (u_p - \theta^{*T} w) \\
 y_p &= C_{pe} x_{pe}
 \end{aligned}
 \tag{18}$$

where x_{pe} is an extended state vector defined by $[x_p, w_1, w_2]^T$, θ^* is determined by (16), and matrices A_{pe}, B_{pe} , and C_{pe} are defined by

$$A_{pe} \equiv \begin{bmatrix} A_p + \theta_3^* B_p C_p & \theta_1^* B_p & \theta_2^* B_p \\ \theta_3^* C_p & -\lambda + \theta_1^* & \theta_2^* \\ C_p & 0 & -\lambda \end{bmatrix}, \quad B_{pe} \equiv \begin{bmatrix} B_p \\ 1 \\ 0 \end{bmatrix}, \quad C_{pe} \equiv [C_p \quad 0 \quad 0]$$

Note that, when $u_p = \theta_i^* w$, (18) becomes

$$\begin{aligned}
 \dot{x}_{pe} &= A_{pe} x_{pe} + \theta_0^* B_{pe} r \\
 y_p &= C_{pe} x_{pe}
 \end{aligned}$$

Meanwhile, $u_p = \theta_i^* w$ also implies $y_p(s)/r(s) = y_m(s)/r(s)$. Therefore, $\{A_{pe}, \theta_0^*, B_{pe}, C_{pe}\}$ should be a realization of the reference model. In other words, the reference model can be realized by the following state-space expression:

$$\begin{aligned} \dot{x}_{me} &= A_{pe}x_{me} + \theta_0^* B_{pe}r \\ y_m &= C_{pe}x_{me} \end{aligned} \tag{19}$$

where x_{me} is the four dimensional state vector of the aforementioned realization. It can be verified that A_{pe} is asymptotically stable.

3) **Error Equations:** By subtracting the reference model's state-space equation (19) from the plant's state-space equation (18), the state-space equations for state error, controller parameter error, and the tracking error are obtained as follows:

$$\begin{aligned} \dot{e} &= A_{pe}e + B_{pe}(u_p - \theta^{*T}w) = A_{pe}e + B_{pe}\tilde{\theta}^T w \\ e_0 &= C_{pe}e \end{aligned} \tag{20}$$

where e , e_0 , and $\tilde{\theta}$ represent the state error, tracking error (output error), and controller-parameter error, respectively

$$\begin{aligned} e &\equiv x_{pe} - x_{me} \\ e_0 &\equiv y_p - y_m \\ \tilde{\theta} &\equiv \theta - \theta^* \end{aligned}$$

In finding the adaption law for the controller by means of the Lyapunov function, the input-output transfer function of a state error-equation should be strictly positive real (SPR) [21]. However, the transfer function of the realization $\{A_{pe}, B_{pe}, C_{pe}\}$ in (20) is not SPR, because $C_{pe}(sI - A_{pe})^{-1}B_{pe}$ equals $G_m(s)/\theta_0^*$ according to (19) and the relative degree of $G_m(s)$ is two [see (13)], which implies that $G_m(s)/\theta_0^*$ is not SPR [16]. To overcome the aforementioned difficulty, we use the identity $(s + g)(s + g)^{-1} = 1$ for some $g > 0$ and rewrite (20) as

$$\begin{aligned} \dot{e} &= A_{pe}e + B_{pe}\{(s + g)(u_g - \theta^{*T}\phi)\} \\ &= A_{pe}e + B_{pe}\{(s + g)\tilde{\theta}^T\phi\} \\ e_0 &= C_{pe}e \end{aligned} \tag{21}$$

where $u_g = u_p/(s+g)$ and $\phi = w/(s+g)$. The term $(s + g)$ will increase the degree of the numerator to make the relative degree of the transfer function equal to one. Since $u_g = \phi$, the controller can be expressed as $u_p = (s + g)u_g = s\theta^T w + \theta^T \phi + g\theta^T \phi = \dot{\theta}^T \phi + \theta^T (\phi + g\phi) = \dot{\theta}^T \phi + \theta^T w$.

Now introduce

$$\bar{e} = e - B_{pe}\tilde{\theta}^T \phi \tag{22}$$

Then, we can derive

$$\begin{aligned} \dot{\bar{e}} &= A_{pe}\bar{e} + (A_{pe}B_{pe} + gB_{pe})\tilde{\theta}^T \phi \\ e_0 &= C_{pe}\bar{e} + C_{pe}B_{pe}\tilde{\theta}^T \phi. \\ \dot{\bar{e}} &= A_{pe}\bar{e} + B_1\tilde{\theta}^T \phi \\ e_0 &= C_{pe}\bar{e}. \end{aligned} \tag{23}$$

For the new state-error equation (23), its transfer function from $\tilde{\theta}^T \phi$ to e_0 should be the same as the transfer function from $\tilde{\theta}^T \phi$ to e_0 in (21) because (23) is equivalently transformed from (21). Therefore, the realization $\{A_{pe}, B_1, C_{pe}\}$ has the following transfer function:

$$\begin{aligned}
 C_{pe}(sI - A_{pe})^{-1}B_1 &= C_{pe}(sI - A_{pe})^{-1}B_{pe}(s + g) \\
 &= (s + g) \frac{G_m}{\theta_0^*} \\
 &= \frac{k_m}{\theta_0^*} \cdot \frac{s + g}{s^2 + a_m s + b_m}
 \end{aligned} \tag{24}$$

where the positive constant g is chosen to be less than a_m . It can be shown that (24) is SPR for any g satisfying $0 < g < a_m$.

4) **Derivation of the Adaptation Law:** To derive the adaptation law for controller parameters, we construct a Lyapunov function that has two error vectors—the controller parameter error $\tilde{\theta}$ and the state error \bar{e}

$$V(\tilde{\theta}, \bar{e}) = \frac{\bar{e}^T P \bar{e}}{2} + \frac{\tilde{\theta}^T \Gamma^{-1} \tilde{\theta}}{2} \tag{25}$$

where Γ is an arbitrary symmetric positive definite matrix and P is a symmetric positive definite matrix determined using Meyer–Kalman–Yakubovich (MKY) Lemma [22]. According to MKY Lemma, since A_{pe} is stable and $\{A_{pe}, B_1, C_{pe}\}$ is a realization of the SPR transfer function (24), there exist a symmetric positive definite matrix P , a vector q , and a scalar $\nu > 0$ such that for any given symmetric positive definite matrix L . Matrix P in (25) satisfies (26).

$$\begin{aligned}
 PA_{pe} + A_{pe}^T P &= -qq^T - \nu L \\
 PB_1 &= C_{pe}^T
 \end{aligned} \tag{26}$$

The time-derivative of the Lyapunov function (25) along the solution of (23) can be calculated as

$$\dot{V}(\tilde{\theta}, \bar{e}) = -\frac{1}{2} \bar{e}^T qq^T \bar{e} - \frac{\nu}{2} \bar{e}^T L \bar{e} + \bar{e}^T P B_1 \tilde{\theta}^T \phi + \tilde{\theta}^T \Gamma^{-1} \dot{\tilde{\theta}}$$

Since $\bar{e}^T P B_1 = \bar{e}^T C_{pe}^T = e_0$, we can choose

$$\dot{\tilde{\theta}} = \dot{\tilde{\theta}} = -\Gamma e_0 \phi \tag{27}$$

so that

$$\dot{V}(\tilde{\theta}, \bar{e}) = -\frac{1}{2} \bar{e}^T qq^T \bar{e} - \frac{\nu}{2} \bar{e}^T L \bar{e} \leq 0. \tag{28}$$

Under the adaptation law (27), the condition (28) will always be satisfied, which guarantees that the tracking error and control parameter error are both stable and bounded. According to the derivations above, the overall MRAC rules can be concluded as follows:

$$\begin{cases}
 \dot{w}_1 = -\lambda w_1 + u_p \\
 \dot{w}_2 = -\lambda w_2 + y_p \\
 \dot{\phi} = -g\phi + w, \quad w = [r, w_1, w_2, y_p]^T \\
 u_p = \theta^T w + \dot{\theta}^T \phi = \theta^T w - \phi^T \Gamma e_0 \phi \\
 \dot{\theta} = -\Gamma e_0 \phi.
 \end{cases} \tag{29}$$

4. SIMULATION RESULTS AND DISCUSSION

The adaptive controller presented in Section III was then simulated for verification. The plant model was chosen to deliver an actual array voltage with an underdamped step response. The reference model was designed to

deliver a theoretical MPP voltage with a critically damped step response. Its damping ratio, which equals $\zeta = \frac{a_m}{2\sqrt{b_m}}$, is the determining factor as inferred from (13). Normally, the ratio is chosen to be either exactly 1 or slightly less than 1. In the latter case, the step response rises faster at the cost of slight overshoot. The desired outcome of simulation would be that after the plant has undergone the adaptation phase, the parameters of the controlled plant would converge to the parameters of the reference model and thus the adapted array voltage would show critically damped behavior.

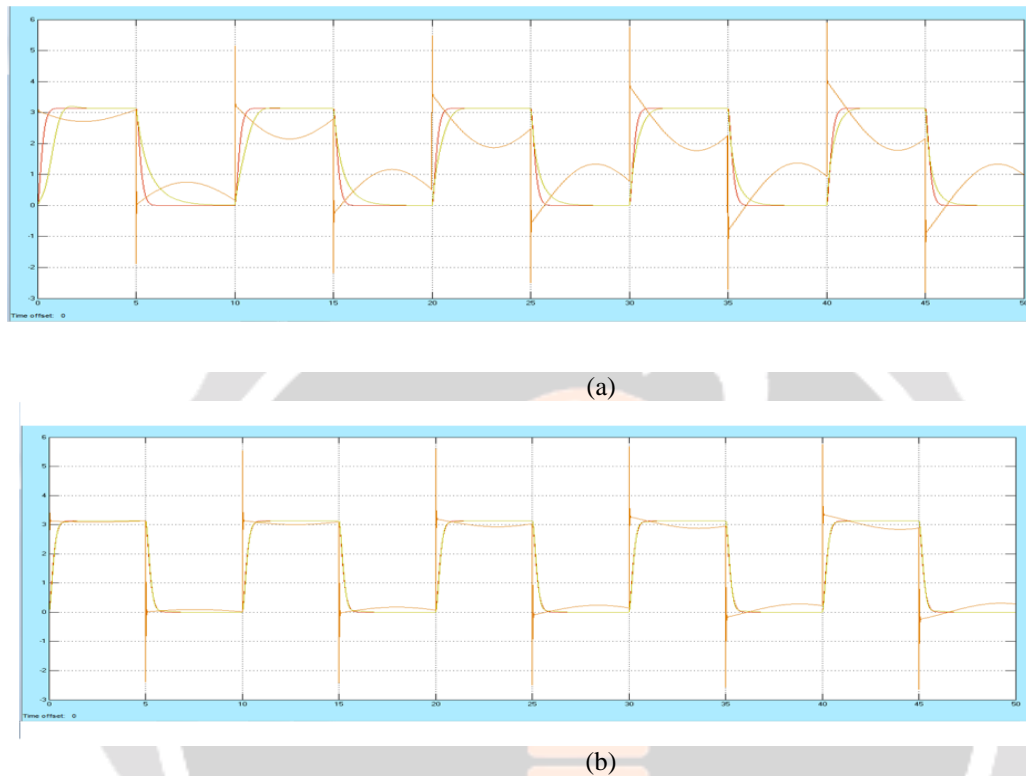


Fig- 8: Comparison of theoretical MPP voltage, adapted array voltage, and unadapted array voltage. The input is a square pulse width modulated signal. (a) Early adaptation stage. (b) Middle adaptation stage.

Fig. 8 shows a comparison between the actual adapted array voltage (using MRAC) and the theoretical MPP voltage, where a square pulse width modulated signal is used to simulate the continued updating of the duty cycle due to the variance in solar insolation. For comparison purpose, Fig. 8 also shows the unadapted array voltage (without using MRAC). The scale in Fig. 8 and subsequent figures has been normalized to an interval between 0 and 1 V. The adapted array voltage oscillates considerably more than both the theoretical MPP voltage as well as the unadapted array voltage. The plant starts to learn and the adapted array voltage begins to dampen while the unadapted array voltage continues to oscillate. Eventually, both the adapted array voltage and the unadapted array voltage reach the theoretical steady-state MPP voltage. This demonstrates the accuracy of RCC and its ability to calculate the correct optimal duty cycle which can deliver maximum available power in the steady state. Then the solar insolation changes and the unadapted voltage shows an under damped response. At this point, the adapted voltage also diverges slightly away from the theoretical MPP. This change in solar insolation represents the first time the ambient conditions have changed after the adapted array voltage has reached a steady-state value. Thus, the plant must learn to adapt to such a change in solar insolation. However, the adapted array voltage in Fig. 8(a) shows no oscillatory response even after the first change in sunlight. That is one of the goals of this study, which is to eliminate any potential underdamped response by the plant due to rapid changes in solar insolation. Next, the adapted array voltage should continue to learn, and converge to the theoretical MPP during the transient changes in solar insolation as shown in Fig. 8(b). In the middle stage of adaptation shown in Fig. 8(b), the adapted array voltage has almost completely converged to the theoretical MPP, even during changes in solar insolation. Conversely, the unadapted array voltage continues to oscillate at each change in solar insolation. In observing the solar array characteristics seen in Fig. 1, it can be inferred that during changes in solar insolation, the unadapted array voltage

fluctuates to the left and right of the MPP, before finally reaching the MPP. On the other hand, the adapted array voltage converges directly to the theoretical MPP with no fluctuation.

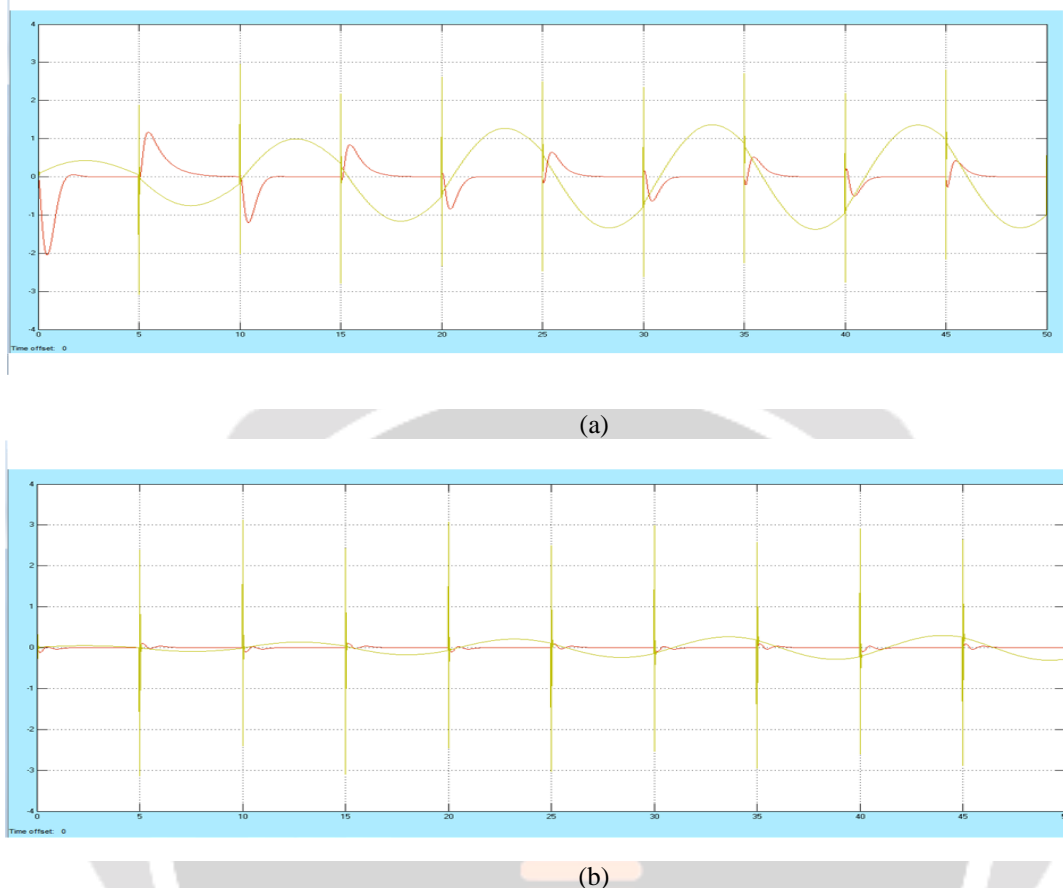


Fig- 9: Error between theoretical MPP voltage and adapted array voltage due to a square pulse-width modulated signal. (a) Early adaptation stage. (b) Middle adaptation stage.

The observations from Fig. 8 are supplemented in Fig. 9, where the error between the actual adapted array voltage and the theoretical MPP voltage is shown. The error between the unadapted array voltage and theoretical MPP voltage is also shown in Fig. 9. As seen in Fig. 9(a), in the early control stage the error for the adapted array voltage is significant. This is consistent with the violent oscillations observed in the adapted array voltage seen in Fig. 8(a). However, after the initial learning phase, the error between the adapted array voltage and theoretical MPP voltage converges to zero in the steady state. As previously stated, the solar insolation changes and there is a transient error in both the adapted array voltage as well as the unadapted array voltage. Comparatively, the error for the adapted array voltage is smaller in magnitude and time duration. Then in the middle stage of adaptation shown in Fig. 9(b), the adapted array voltage error during each transient change in solar insolation is significantly smaller than seen in the initial phase. Conversely, the unadapted array voltage error continues to oscillate with a larger magnitude and time-duration than the adapted array voltage.

5. CONCLUSION

In order to improve the efficiency of photovoltaic systems, MPPT algorithms are used, aiming to deliver the maximum available power from the solar array to the load. Critical issues to be considered in the MPPT algorithms include system complexity, uncertainty, and dynamical performance. This paper developed a two-level adaptive control architecture that can reduce complexity in system control and effectively handle the uncertainties and perturbations in the photovoltaic systems and the environment. The first level of control was RCC, and the second level was MRAC. This paper focused mostly on the design of the MRAC algorithm, which compensated the underdamped characteristics of the power conversion system. In a sequel paper, we will provide a comprehensive analysis validating the coupling of MRAC with RCC.

REFERENCES

- [1] S. L. Brunton, C. W. Rowley, S. R. Kulkarni, and C. Clarkson, "Maximum power point tracking for photovoltaic optimization using ripple-based extremum seeking control," *IEEE Trans. Power Electron.*, vol. 25, no. 10, pp. 2531–2540, Oct. 2010.
- [2] R. A. Mastromauro, M. Liserre, T. Kerekes, and A. Dell'Aquila, "A singlephase voltage-controlled grid-connected photovoltaic system with power quality conditioner functionality," *IEEE Trans. Ind. Electron.*, vol. 56, no. 11, pp. 4436–4444, Nov. 2009.
- [3] A. K. Abdelsalam, A. M. Massoud, S. Ahmed, and P. N. Enjeti, "High-performance adaptive perturb and observe MPPT technique for photovoltaic-based microgrids," *IEEE Trans. Power Electron.*, vol. 26, no. 4, pp. 1010–1021, Apr. 2011.
- [4] M. A. Elgendy, B. Zahawi, and D. J. Atkinson, "Assessment of perturb and observe MPPT algorithm implementation techniques for PV pumping applications," *IEEE Trans. Sustainable Energy*, vol. 3, no. 1, pp. 21–33, Jan. 2012.
- [5] G. Petrone, G. Spagnuolo, and M. Vitelli, "A multivariable perturb-and-observe maximum power point tracking technique applied to a singlestage photovoltaic inverter," *IEEE Trans. Ind. Electron.*, vol. 58, no. 1, pp. 76–84, Jan. 2011.
- [6] S. Jain and V. Agarwal, "A new algorithm for rapid tracking of approximate maximum power point in photovoltaic systems," *IEEE Power Electron. Lett.*, vol. 2, no. 1, pp. 16–19, Mar. 2004.
- [7] N. Femia, G. Petrone, G. Spagnuolo, and M. Vitelli, "Optimization of perturb and observe maximum power point tracking method," *IEEE Trans. Power Electron.*, vol. 20, no. 4, pp. 963–973, Jul. 2005.
- [8] M. A. S. Masoum, H. Dehbonei, and E. F. Fuchs, "Theoretical and experimental analyses of photovoltaic systems with voltage and current-based maximum power-point tracking," *IEEE Trans. Energy Convers.*, vol. 17, no. 4, pp. 514–522, Dec. 2002.
- [9] T. Esumi and P. L. Chapman, "Comparison of photovoltaic array maximum power point tracking techniques," *IEEE Trans. Energy Convers.*, vol. 22, no. 2, pp. 439–449, Jun. 2007.
- [10] M. Veerachary, T. Senjyu, and K. Uezato, "Neural-network-based maximum-power-point tracking of coupled-inductor interleaved-boost-converter-supplied PV system using fuzzy controller," *IEEE Trans. Ind. Electron.*, vol. 50, no. 4, pp. 749–758, Aug. 2003.
- [11] P. T. Krein, "Ripple correlation control, with some applications," in *Proc. IEEE Int. Symp. Circuits Syst.*, 1999, vol. 5, pp. 283–286.
- [12] D. L. Logue and P. T. Krein, "Optimization of power electronic systems using ripple correlation control: A dynamic programming approach," in *Proc. IEEE 32nd Annu. Power Electron. Special. Conf.*, 2001, vol. 2, pp. 459–464.
- [13] J. W. Kimball and P. T. Krein, "Discrete-time ripple correlation control for maximum power point tracking," *IEEE Trans. Power Electron.*, vol. 23, no. 5, pp. 2353–2362, Sep. 2008.
- [14] T. Esumi, J. W. Kimball, P. T. Krein, P. L. Chapman, and P. Midya, "Dynamic maximum power point tracking of photovoltaic arrays using ripple correlation control," *IEEE Trans. Power Electron.*, vol. 21, no. 5, pp. 1282–1291, Sep. 2006.
- [15] D. E. Miller, "A new approach to model reference adaptive control," *IEEE Trans. Autom. Control*, vol. 48, no. 5, pp. 743–757, May 2003.
- [16] S. Sastry and M. Bodson, *Adaptive Control: Stability, Convergence and Robustness*. New York: Dover Publications, 2011.
- [17] E. V. Solodovnik, S. Liu, and R. A. Dougal, "Power controller design for maximum power tracking in solar installations," *IEEE Trans. Power Electron.*, vol. 19, no. 5, pp. 1295–1304, Sep. 2004.
- [18] A. D. Rajapakse and D. Muthumuni, "Simulation tools for photovoltaic system grid integration studies," in *Proc. Electr. Power Energ. Conf. (EPEC 2009)*, Oct., pp. 1–5. [19] T. Messo, J. Jokipii, and T. Suntio, "Steady-state and dynamic properties of boost-power-stage converter in photovoltaic applications," in *Proc. 3rd IEEE Int. Symp. Power Electron. Distrib. Generat. Syst. (PEDG 2012)*, Jun., pp. 34–40.
- [20] L. Nousiainen, J. Puukko, A. Maki, T. Messo, J. Huusari, J. Jokipii, J. Viinamaki, D. T. Lobera, S. Valkealahti, and T. Suntio, "Photovoltaic generator as an input source for power electronic converters," *IEEE Trans. Power Electron.*, vol. 28, no. 6, pp. 3028–3038, Jun. 2013.
- [21] P. Inoannou and J. Sun, *Robust Adaptive Control*. Englewood Cliffs, NJ: Prentice Hall, 1996.
- [22] K. R. Meyer, "On the existence of Lyapunov functions for the problem on Lur'e," *J. SIAM, Series A: Contr.*, vol. 3, no. 3, pp. 373–383, Aug. 1965.